PERGAMON

Journal of Structural Geology 23 (2001) 777–788

JOURNAL OF STRUCTURAL GEOLOGY

www.elsevier.nl/locate/jstrugeo

Pressure anomalies around cylindrical objects in simple shear

V. Tenczer[a,*], K. Stüwe[a], T.D. Barr[b]

[a]*Department of Geology and Paleontology, Karl-Franzens-University of Graz, Heinrichstrasse 26, 8010 Graz, Austria*
[b]*AFEX International, Echo Lane, Houston, TX, USA*

Received 17 May 2000; accepted 13 October 2000

Abstract

We model the pressure distribution around cylindrical objects in simple shear deformation using the finite element method in two dimensions and present an analytical solution for a special case. Parameter space is explored numerically for viscosity contrast between object and matrix, η, and for the non-linearity of flow, as expressed by n. We show that the geometry and size of the pressure shadow is independent of η, but strongly dependent on n. For example, at $n = 1$, pressure shadows are roughly circular in shape, while for $n > 1$, pressure shadows disintegrate into two branches. We also show that pressure may only exceed 100 MPa in pressure shadows at resolvable distances from the object if $\eta > 4$ for strain rates of 10^{-14} s^{-1} and matrix viscosities around 10^{22} Pa s. As these values for strain rate, viscosity and viscosity contrast are geologically reasonable, we emphasise that it is conceivable that geobarometric results obtained from syndeformational mineral parageneses near rigid porphyroblasts may be influenced by non-lithostatic components of pressure. © 2001 Elsevier Science Ltd. All rights reserved.

1. Introduction

The magnitude of the flow stresses in the Earth's crust is one of the most important parameters governing dynamical processes in continents. Accordingly, many authors have attempted to constrain their magnitude. There has been some debate about their magnitude, however, ranging from studies attributing a significant contribution of 'tectonic overpressures' to the formation of metamorphic parageneses (Rutland, 1965; Ernst, 1971; Mancktelow, 1993; Petrini and Podladchikov, 2000) to those studies that have concluded that differential stresses are negligible for the barometric interpretation of metamorphic rocks (e.g. Gleason and Tullis, 1995). Some studies have shown, however, that even small differential stresses can be relevant for the interpretation of metamorphic parageneses under some circumstances (Stüwe and Sandiford, 1994). Despite this active debate, most petrological studies now assume that the stress state of the Earth is near lithostatic and barometric results can be translated directly into the crustal depth of metamorphism.

Despite this assumption, there is abundant evidence in rocks that stresses, and therefore pressures vary on a local scale. For example, the existence of pressure shadows, strain caps, strain fringes, winged porphyroclasts and delta objects all testify to the existence of local stress fluctuations. Indeed, *any* fabric development would be impossible without local stress variations and a number of authors have discussed the stresses during heterogeneous deformation on a local scale, for example during folding (Strömgård, 1974) or boudinage (Strömgård, 1973; Selkman, 1978). Palaeopiezometric studies have attempted to constrain the magnitude of such local stress variations in rocks using a variety of observations, for example grain size (Edward et al., 1982; Koch, 1983). Such paleopiezometric studies are generally performed using single phase rocks. Most observations on local pressure variations are made in polyphase rocks, however, for example observations on the formation of mineral parageneses in pressure shadows behind porphyroblasts (Fig. 1). Observations of this sort pose the question how large these pressure shadows are. An answer to this question will be of direct relevance to any geobarometric interpretation of reaction textures like those shown in Fig. 1.

In this paper we evaluate the geometry, size and magnitude of pressure shadows around cylindrical objects in order to contribute to this debate. This general theme has been dealt with in the past (Shimamoto, 1975; Masuda and Ando, 1988; Masuda et al., 1995; Masuda and Mizuno, 1996; Pennacchioni et al., 2000). The studies of Masuda and his co-authors, however, have assumed an infinite rheology

* Corresponding author. Tel.: +43-316-380-5681; fax: +43-316-380-9870.

E-mail addresses: tenczer@kfunigraz.ac.at (V. Tenczer), kurt.stuewe@kfunigraz.ac.at (K. Stüwe), tdbarr@afexintl.com (T.D. Barr).

0191-8141/01/$ - see front matter © 2001 Elsevier Science Ltd. All rights reserved.
PII: S0191-8141(00)00155-3

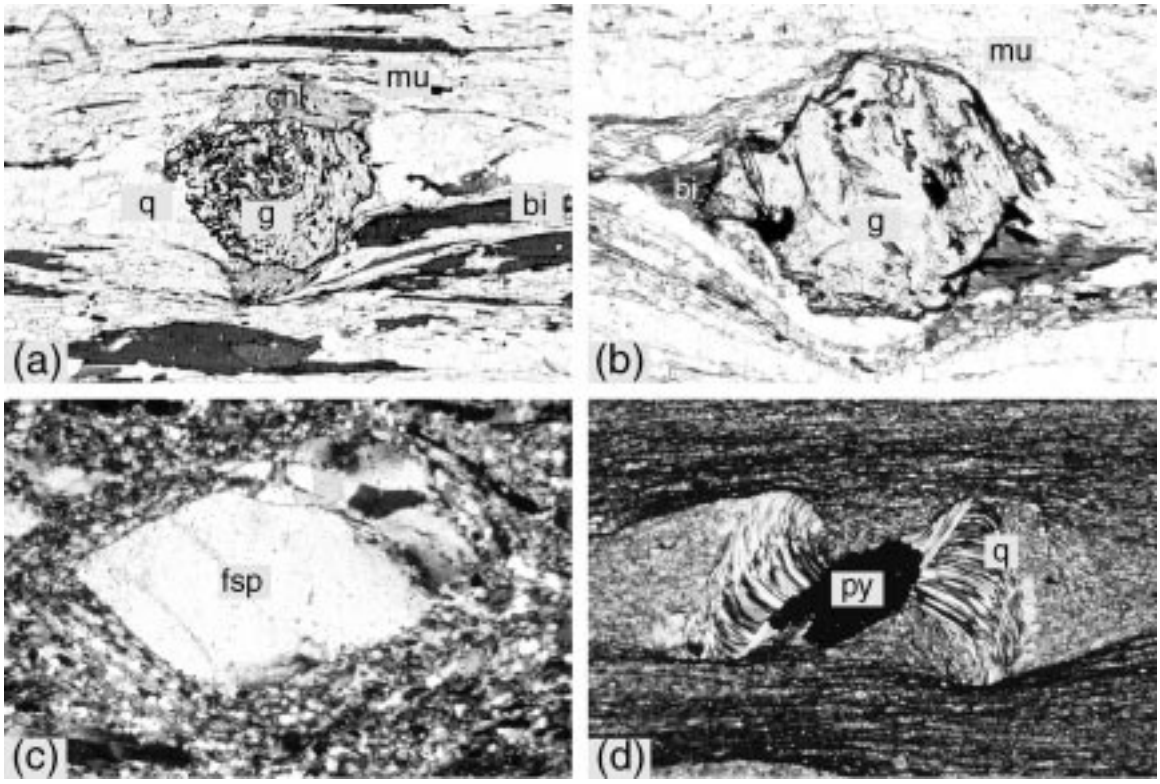

Fig. 1. Photomicrographs of natural examples of 'pressure shadows' around porphyroblasts. (a) Micaschist from the high Himalayan crystalline complex, central Bhutan showing chlorite growing as 'strain caps' on a rigid garnet porphyroblast. The slightly asymmetric 'pressure shadow' is filled with quartz. Length of photo is 5 mm. (b) Example from the Plattengneiss shear zone, Austroalpine. A garnet crystal is surrounded by a slightly asymmetrically-oriented pressure shadow of biotite. Length ca. 0.5 mm. (c) Recrystallisation tails on feldspar porphyroclast from the Plattengneiss. Length of photo is 3.5 mm. Crossed Nicols. (d) Pressure fringe on a pyrite grain, filled with quartz. Length of the fringe ca. 10 mm. Crossed Nicols. Mineral abbreviations are: mu = muscovite, g = garnet, bi = biotite, q = quartz, chl = chlorite, fsp = K-feldspar, py = pyrite.

contrast between object and matrix. This is in contrast with many observations in real rocks which almost always show that the objects around which pressure shadows form may also behave in a ductile manner (e.g. Ji and Martignole, 1994; Passchier and Trouw, 1996). Thus, we explore here the pressure distribution around objects of a *finite* rheology contrast with the matrix. Moreover, some geologically relevant aspects of the geometry of pressure shadows in non-linear rheologies are only implicit in the results of Masuda, but are not discussed or explained there. Other studies concerned with the numerical evaluation of pressures around cylindrical objects, have focused on: (i) the effects of the geometry of the object (Selkman, 1983), (ii) the influence of compaction (McKenzie and Holness, 2000), (iii) the effects of coupling between object and matrix (Kenkmann and Dresen, 1998; Kenkmann, 2000), or (iv) the flow field around the object without any consideration of the pressure field (Pennacchioni et al., 2000). Some of these studies have used experimentally-derived flow laws as a constitutive relationship and usually assumed constant boundary conditions when exploring various power law exponents. Both assumptions make it difficult to compare the behaviour of linear and non-linear viscous rheologies because they imply a variable effective viscosity in the far field. Here we expand on these previous studies by presenting a careful evaluation (and comparison) of the effects of: (i) the non-linearity of the rheological behaviour, and (ii) the effective viscosity contrast. We also present a detailed physical explanation of various aspects of the geometry of pressure distribution, which has not been performed by other studies.

2. Model formulation

For the calculation of pressures in the vicinity of objects or inclusions, we use the finite element code BASIL by Houseman, Barr and Evans (Barr and Houseman, 1996; Bons et al., 1997; see also www.earth.monash.edu.au/Research/Basil). This program solves the force balance equations in two dimensions. These may be written as:

$$\frac{\delta}{\delta c_j}\tau_{ij} + \frac{\delta}{\delta c_i}P = 0 \tag{1}$$

where c is a coordinate in space, the i and j subscripts represent the x or y directions and τ_{ij} is the deviatoric stress tensor. P is pressure and is defined as the mean principle stress: $P = (\sigma_1 + \sigma_2)/2$. Within the sign convention of

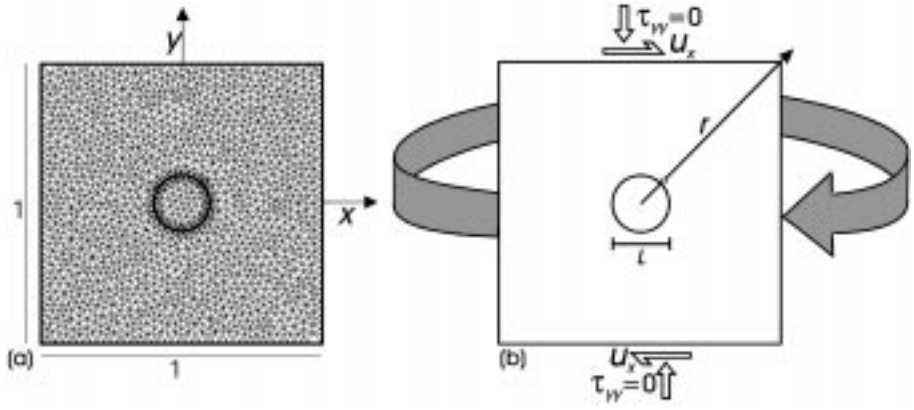

Fig. 2. Model set up used in this paper. (a) Mesh and coordinate system. (b) Boundary conditions for the simulation of simple shear deformation. The axis r will be used to interpret pressure profiles in the shadows. Coordinates of r may also be given $\sqrt{x^2 + y^2}$. The white dot along the r-axis near the object contact indicates the location where we define P_{max}.

Eq. (1), compressive stresses are negative and tensile stresses are positive. This is opposite to the common geological convention for the sign of stresses but will be used here. Thus, pressures are *positive* in the 'pressure shadows'. Also, note that all pressures are given relative to a far field pressure of zero.

In order to assign a deformation field to the stresses obtained from Eq. (1) we assume that rocks can be described as a viscous fluid. This assumption is justified for processes that occur on a larger than sub-grain scale where individual crystal flow laws must be considered. For an incompressible medium viscous behaviour may then be described by a constitutive relationship in which stress and strain rate are related by the relationship:

$$\tau_{ij} = B\dot{E}^{\left(\frac{1}{n}-1\right)}\dot{\epsilon}_{ij} \tag{2}$$

where $\dot{\epsilon}_{ij}$ is the strain rate tensor, $\dot{E}$ is the second invariant of the strain rate tensor and n is a power law exponent describing the non-linearity of the proportionality between stress and strain rate. Strain rate is defined as:

$$\dot{\epsilon}_{ij} = \frac{1}{2}\left(\frac{\delta u_i}{\delta c_j} + \frac{\delta u_j}{\delta c_i}\right) \tag{3}$$

where u is the velocity in either the x or the y direction. Note that Eq. (2) describes a stress–strain rate relationship which is isotropic with respect to strain rate. It is therefore different from other possible descriptions of viscous behaviour, for example: $\tau_{ij} = B\dot{\epsilon}_{ij}^n$. B is a scalable constant that contains information about material constants and their temperature dependence (England and McKenzie, 1982). If $n = 1$, Eq. (2) reduces to $\tau_{ij} = B\dot{\epsilon}_{ij}$ and B is identical to viscosity, $B \equiv \eta$, and has the units of Pa s. Then, the pressure distribution in the shadow may be evaluated analytically (see Appendix A) and we compare our numerical results with this solution. For non-linear viscous rheologies, B is only a pre-exponent constant and the viscosity is strain rate dependent. Then, it is only possible to define an *effective viscosity* given by the ratio of stress to strain rate. From Eq. (2), this is given by:

$$\eta = B\dot{E}^{\left(\frac{1}{n}-1\right)}. \tag{4}$$

Note that the abbreviation η is used for viscosity if $n = 1$ and for *effective viscosity* if $n \neq 1$.

For linear viscous materials, the viscosity *contrast* between two different materials is given by the ratio of their viscosities, or the ratio of the constant B. In the calculations presented below we always assume that the matrix viscosity is one, so that the viscosity contrast is given directly by η.

For non-linear rheologies, the effective viscosity depends on strain rate (Eq. (4)) and the viscosity contrast will be different in different areas if they deform at different strain rates, or under different stresses. We define the viscosity contrast between two materials for a stress state where both deform under the same stress. Then, it can be shown from Eq. (2) that the viscosity contrast is given by:

$$\eta = B^n. \tag{5}$$

For example, if the rheology contrast between a matrix and an inclusion is set to 100 and $n = 1$, then: $B = 100$. If $n = 3$, then: $B = 100^{(1/3)} = 4.642$.

Our model solves the mechanical behaviour of an object that is circular in shape in a matrix of infinite extent in two dimensions. Limitations of the model include: (i) a variation of n in space leading to a transition between deformation mechanisms e.g. volume creep and grain boundary sliding (Frost and Ashby, 1982) and a variation of η. (ii) We did not take into account the formation of clusters or the interaction between different objects (see Biermeier et al., 2000). (iii) Our model neglects the possiblity of mechanical strengthening around the rigid phase caused by the presence of the inhomogeneity.

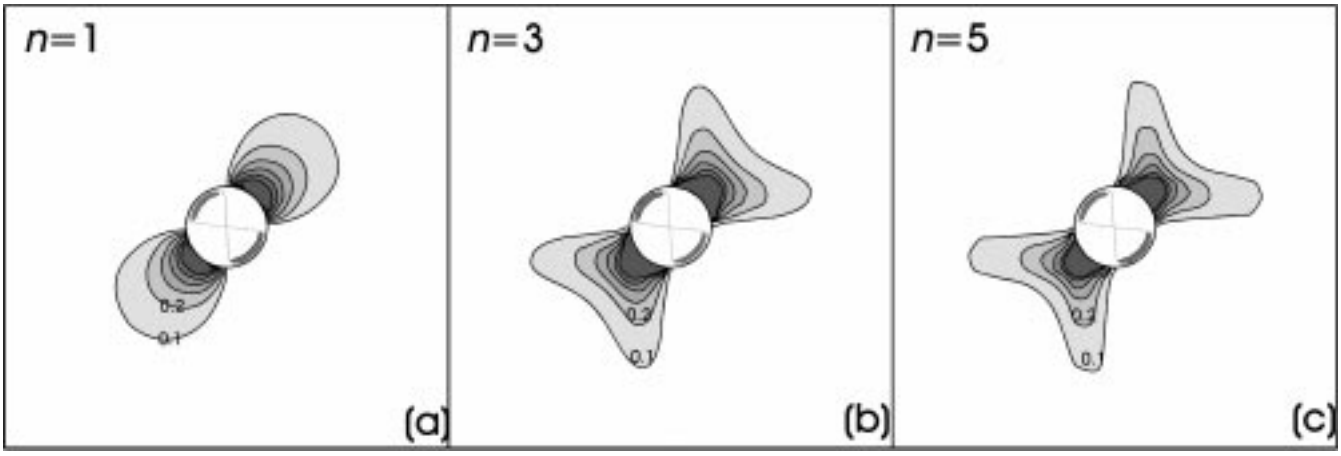

Fig. 3. Geometry of the pressure distribution for three different power law exponents labelled on the diagrams. The contours are independent of η and are shown as fractions of P/P_{max} between 0.1 and 0.6.

2.1. Meshing and geometry

In our numerical experiments we deformed a square box with the side length 1 centred around the origin of a Cartesian coordinate system with the axes x and y as shown in Fig. 2(a). 164 grid nodes were defined in regular intervals along the circumference of this box. In the centre of the box, a circular region of diameter $L = 0.2$ was defined by 80 coordinates. This size gives a good approximation of the behaviour of pressure anomalies around circular objects in a matrix of infinite extent (Biermeier et al., 2000; Pennacchioni et al., 2000; and also discussion Section 4.2). This geometry was triangulated with a self-triangulation routine using Delaunay triangles which were allowed a maximum area of 0.0005 and a minimum angle of 20°. The choice of triangle size and numbers of nodes along the circumference of the circular region corresponds to a numerical resolution of about 30 μm if scaled to a porphyroblast size of 1 mm. This is roughly equal to the resolution of optical and electron microprobe methods and suffices therefore for most geological purposes. A single additional node was inserted at $x = 0.07212$ and $y = 0.07212$, which is located at a distance of $L/100$ from the contact of the inclusion at 45° to the shear zone boundary (Fig. 2(b)). For a scaled porphyroblast size of 1 mm diameter, this corresponds to a distance of 10 μm from its contact. The circular region was assigned a variable value of B and is assumed to be fully-coupled to the matrix. The entire region of the box was assigned a power law exponent n. As the matrix value for B is assumed to be one, the assigned B value for the circular region is the pre-exponent rheology contrast of the inclusion relative to the matrix and the effective viscosity contrast to the matrix is given by Eq. (5).

2.2. Boundary conditions and explored parameter space

In order to deform the initial geometry described above, we assume the following boundary conditions. At the top (at $y = 0.5$) we prescribe a constant velocity in the x direction of $u_x = 0.5$ in the dimension of length unit per time unit. At the bottom of the box (at $y = -0.5$) we prescribe a velocity of the boundary of $u_x = -0.5$ (Fig. 2(b)). According to our definition of strain rate in Eq. (3), this corresponds to a far-field shear strain rate of $\dot{\epsilon}_{xy} = 0.5$. In the y direction, we prescribe a constant stress boundary condition at the top and bottom boundaries. Thus, the top and bottom boundaries are allowed to move in the y direction in response to the stress arising around the circular region in the centre of the grid. This boundary condition approximates ideal simple shear only in the far field beyond the described region, but gives the best approximation to simulate the stress state of porphyroblasts in a matrix of infinite extent (see discussion Section 4.2).

The side boundaries are defined by the condition that both components of traction and both components of velocity are continuous from one side to the other side. This assumption of a periodic boundary is analogous to deformation experiments in a ring shear apparatus. For a meaningful comparison of linear and non-linear rheologies, velocity boundary conditions and all results were scaled, so that the integrated shear stress along the boundaries are always the same (see Section 4.1).

We explored the stress state of cylindrical objects and their surroundings for the viscosity contrast between object and matrix and for the non-linearity of the viscous behaviour as described by n. The variability of the results was also explored as a function of object size and boundary conditions. All numerical experiments were performed for finite deformation, but we confine our discussion largely to the results of the incremental time step. All results are presented in non-dimensional form, so that they are independent of experimentally-derived material constants. Their geological scaling is discussed in Section 4.1.

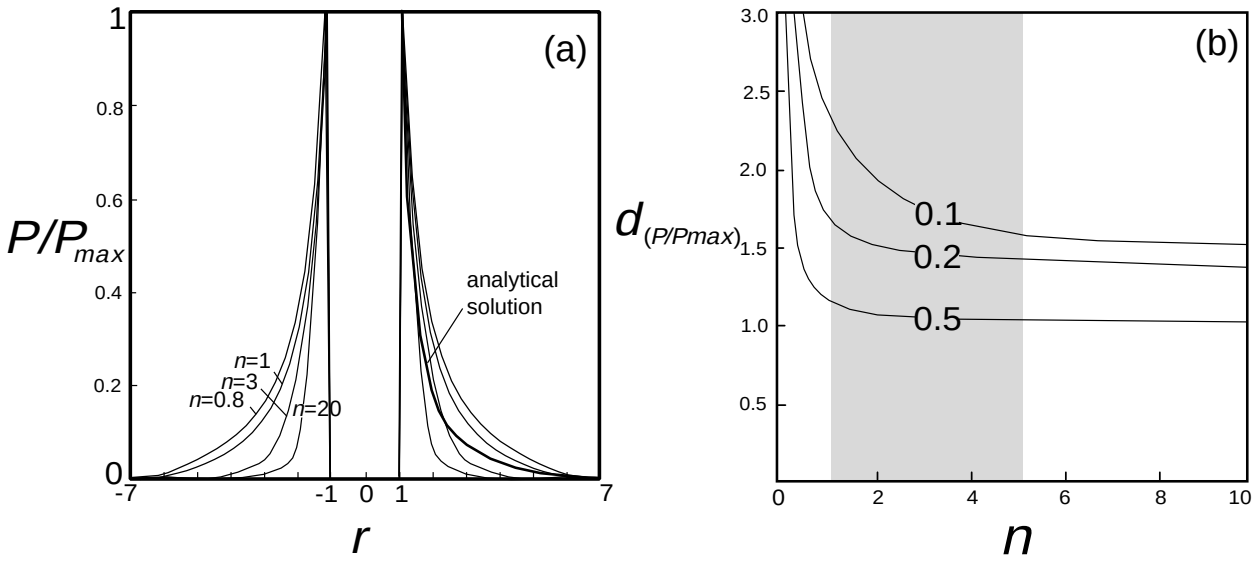

Fig. 4. (a) Pressures normalised against P_{max} as a function of r (distance from the object centre) in units of $L/2$. Curves are shown for values of n between 0.8 and 20. r is labelled in units of $L/2$ measured from the centre of the inclusion. (b) The size of the pressure shadow d measured in direction of r as a function of n. The subscript (P/P_{max}) indicates that d is measured in terms of the P/P_{max} ratio. Curves are shown for $P/P_{max} = 0.1$, 0.2 and 0.5. The shaded region shows the geologically relevant range of n.

3. Results

The pressure field around the circular objects may be characterised by three parameters: (1) the spatial *geometry* of the pressure field—in particular that of the pressure shadows; (2) the spatial *size* of the pressure shadows; and (3) the *magnitude* of the pressure in and around the circular object. The results are discussed in terms of these three aspects.

3.1. Geometry of the pressure distribution

Fig. 3 shows the distribution of pressure around circular inclusions for three different n at the incremental time step. Pressures are shown as fractions of the pressure maximum on the boundary of the object. For the purpose of defining a geologically meaningful pressure maximum, we define as P_{max} the pressure of the additional grid node, defined in Section 2.1. This is located at $L/100$ from the inclusion contact and is therefore of the order of optical resolution that may be obtained in thin section (Fig. 2(b)). A theoretical P_{max} for the case where $n = 1$ may also be obtained from the analytical solution presented in Appendix A. The pressure contours outside the circular inclusion correspond to what is loosely-called 'pressure shadows' and will be the principle focus of our attention. Fig. 3 is independent of the viscosity contrast, as the geometry of the pressure shadow depends only on the geometry of the object boundary and not its viscosity contrast. For clarity, only the pressures in the quadrants of the 'pressure shadows' are shown, but it is understood that the pressure distribution is symmetric about the inclusion. Thus, corresponding pressure contours (of opposite sign) would appear in this figure in the top left and bottom right quadrants. Textural evidence for pressure anomalies there, is often referred to (not quite correctly) as 'strain caps'.

Fig. 3 shows that the pressure distribution around the inclusion is characterised by a continuous drop of pressure along lines extending radially from the inclusion contact. At contact, there is a discontinuity in the pressure field (see Appendix A). During linear viscous deformation ($n = 1$) pressure shadows have a roughly circular shape. For non-linear rheologies, the pressure shadows disintegrate into two branches that extend at roughly 20 and 70° to the shear zone boundaries, respectively. In these two directions, the pressure shadows are actually *longer* than for the linear case, while in the direction of the maximum pressure of linear rheologies (45° to the shear zone boundary), the pressure shadows become *shorter* for larger n. This effect becomes stronger for larger n. In the following, we refer to the shape of pressure shadows at large n, as in Fig. 3(b) and (c), as 'bone-shaped'. The difference of pressure geometry as a function of n arises because of small differences in the flow-field between linear and non-linear rheologies. Masuda and Mizuno (1996; figs. 4 and 5) and Pennacchioni et al. (2000; fig. 3c) showed that differences in the flow-field *do* exist, but were not aware of their importance to the geometry of the pressure shadows and thus, refrained from interpreting their significance. In essence the different geometries of the pressure shadows for $n = 1$ and $n > 1$ arise from changes in the u_y component of the velocity field. This has the consequence that the trace of the inflection points of the flow lines

around the object is at steeper angles to the shear zone boundaries for larger n, which ultimately determines the geometry of the pressure field.

3.2. Size of the pressure shadows

The size of the pressure shadows can be best described in a profile through the pressure shadows along the instantaneous stretching axis, oriented at 45° to the shear zone boundaries (r-axis on Fig. 2(b)). Using this axis has also the advantage that the pressure along it can be directly compared with the analytical solution of Eq. (11). Fig. 4(a) shows such pressure profiles for different n. Akin to the geometry of the pressure shadows, these profiles are independent of the viscosity contrast if they are normalised at the maximum pressure P_{max}.

It may be seen that the pressure decreases from P_{max}, along an exponential curve and merges asymptotically into the far-field pressure at large distances from the object. Along this profile, the pressure drops more rapidly for larger n than for smaller n. In comparison with the result of Eq. (11), however, the analytical solution (thick line in Fig. 4(a)) provides a slightly different pressure profile along the r-axis. From P_{max}, the slope of the curve is steeper than for the numerical solution for $n = 1$ and reaches slightly smaller values. This difference may be explained by the resolution of the numerical simulation very close to the boundary of the object (between the exact boundary at $r = 1$ and our reference point 10 μm away from the object). Note that the relationship between pressure as a function of distance and n may be different along different profiles. For example, if we consider the pressure drop along profiles that trace the points of maximum pressure of individual flow lines (i.e. at 22.5° relative to the x-axis), then the pressure would drop more rapidly for small n and slower for large n (Figs. 3 and 4(a)).

Here, however, we continue interpreting profiles along profiles in direction r. In order to define the spatial size of the pressure shadows, we define this by the distance d, where pressure drops below a given ratio of P/P_{max}. For example, if the maximum pressure difference P_{max} relative to the lithostatic pressure is around 2 kbar, then $P/P_{max} = 0.1$ corresponds to 0.2 kbar and implies that within the pressure shadow, pressure is between 2 and 0.2 kbar higher than in the far-field. Values below 0.2 kbar pressure difference belong in this case to the matrix. In Fig. 4(b) d is plotted as a function of n for $P/P_{max} = 0.1$, 0.3 and 0.5. It may be seen that the pressure shadow along this axis extends to very large distances from the inclusion for $n < 1$, but becomes small but constant for large n. Note, however, that d only drops with increasing n, if it is defined by a ratio of P/P_{max} as done here. If it is defined by a given pressure exceeding the matrix pressure (for example by the size of the region where $P > 100$ MPa), then the size of the pressure shadow will depend on η, as well as n. The scaling of the size to real pressure values will be done in Section 4.1.

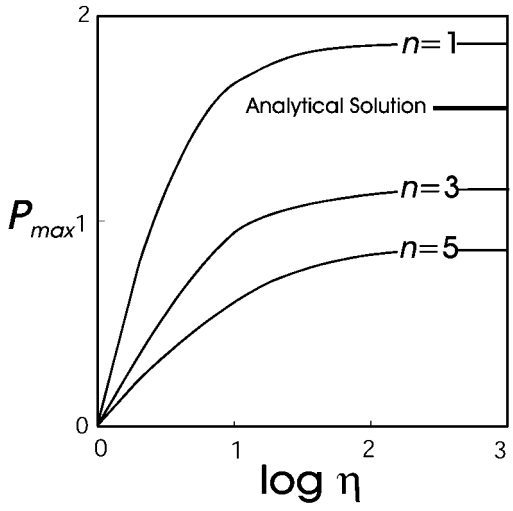

Fig. 5. P_{max} as a function of η (logarithmic plot) for different n. Note that the results for different n are scaled for equal integrated shear stress at the boundaries.

3.3. The magnitude of the pressure shadow

In contrast to the geometry and size of the pressure shadows, the magnitude of pressure is a strong function of the viscosity contrast, η. In Fig. 5 we explore the dependence of P_{max} on η for a range of n. It may be seen that P_{max} increases with increasing viscosity contrast and approaches a constant for $\eta = \infty$. For Newtonian rheologies this constant value is given by Eq. (12). Clearly, at $\eta = 1$, P_{max} is also zero. At small viscosity contrasts, P_{max} increases rapidly with η and the rate of increase of P_{max} with η decreases, even on a logarithmic scale (Fig. 5). The magnitude of P_{max} also depends on n. It is larger for smaller n. Note that this important result is for the assumption that linear and non-linear rheologies may be compared when the integrated shear stresses at the boundaries are equal (see boundary conditions as well as the next section). The shape of the curves is similar for all n and viscosities. For all n more than 90% of the possible P_{max} is reached at $\eta = 100$ ($\log(\eta) = 2$). At much larger η the dimensionless P_{max} reaches asymptotically $P_{max} \approx 0.8$, 1.2 and 1.8, for $n = 5$, 3 and 1, respectively. The maximum curvature of the P_{max} versus $\log(\eta)$-curves is for all n roughly at $\eta = 10$. At high viscosity contrasts the analytical solution is shown as a reference line for the values of P_{max}. The value for $n = 1$ at infinite viscosity contrast is $P_{max} = 1.5$ and differs therefore around 15% from the numerical results.

4. Discussion

4.1. Geological scaling of non-dimensional model results

The geological scaling of the non-dimensional results of Figs. 3–5 is different for linear and non-linear rheologies. For *linear* viscous rheologies, ($n = 1$), it is straightforward.

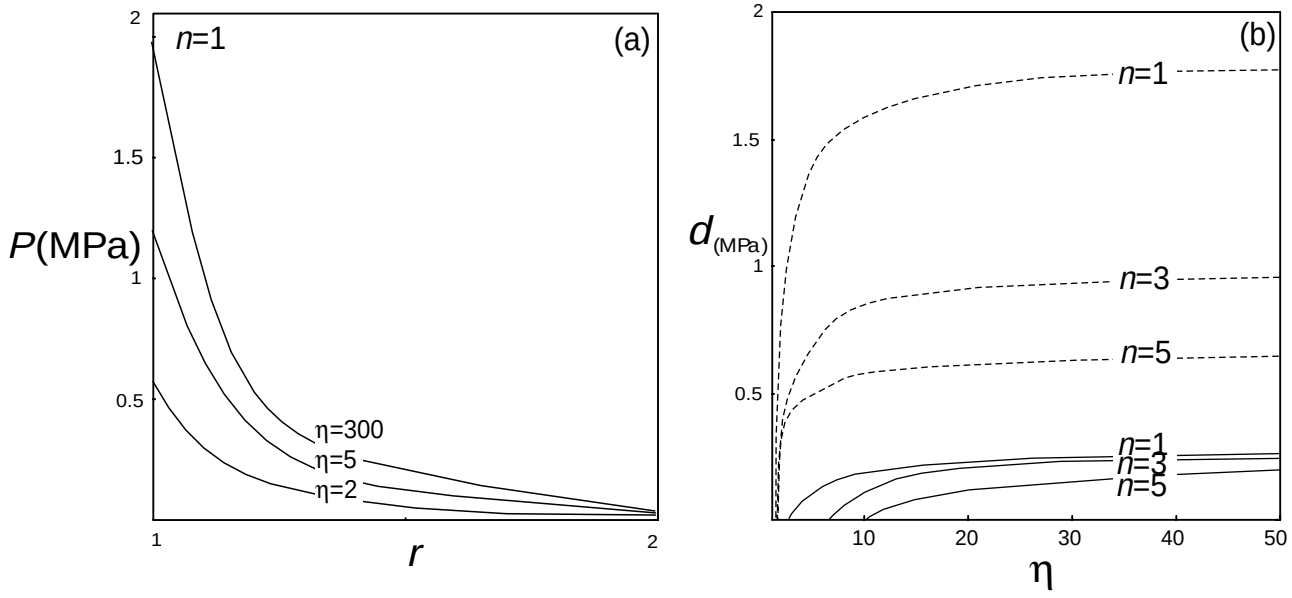

Fig. 6. (a) Pressure as a function of r shown for a range of viscosity contrasts η, at $n = 1$. (b) The size of the pressure shadow $d_{(\mathrm{MPa})}$ measured in direction of r in units of $L/2$ as a function of η. Curves are shown for $n = 1$, 3 and 5. Continuous lines are for $d_{(\mathrm{MPa})}$ where P exceeds 100 MPa, dashed lines are for $d_{(\mathrm{MPa})}$ where P exceeds 10 MPa, both for scaling values of $\eta_g = 10^{22}$ Pa s and $\dot{\epsilon}_g = 10^{-14}$ s^{-1}.

For example, if we choose a non-dimensional model viscosity of $\eta = 1$ to correspond to a geological value of $\eta_g = 10^{22}$ Pa s, and a non-dimensional model strain rate of 1 to correspond to $\dot{\epsilon}_g = 10^{-14}$ s^{-1} then a non-dimensional model pressure of $P = 1$ means a pressure of $P_g = \eta_g \dot{\epsilon}_g =$ 100MPa. The subscript 'g' is used for scaling values so that they are not confused with the non-dimensional values for η or $\dot{\epsilon}_{ij}$ used in Figs. 3–5. Thus, in Fig. 5, a viscosity contrast of 100 and $n = 1$ implies a $P_{\max}$ of about 180 MPa for these scaling factors of strain rate and viscosity assumed above. $\eta = 100$ in the above example also implies that the inclusion has a viscosity of $\eta_g = 10^{24}$ Pa s. Thus, in Fig. 3(a), the 0.1 contour will correspond to 18 MPa for $\eta = 100$.

In Fig. 3(a) the maximum distance of the $P/P_{\max} = 0.1$ contour is located at a distance of $1.3L$ from the inclusion contact, for $n = 1$. However, if the size of the pressure shadow is measured by the distance over which P exceeds a given absolute pressure difference relative to the matrix, then the size of the pressure shadow is strongly dependent on η. To illustrate this, we show in Fig. 6(a) a scaled reproduction of Fig. 4(a) for $n = 1$. This, and equivalent figures for different n may be constructed by combining Figs. 4(a) and 5. In Fig. 6(b), d indicates the distance over which a given pressure is exceeded along r. The subscript 'MPa' indicates that d is measured here in terms of real pressures. It is shown that there is *no* pressure shadow larger than 100 MPa for $n = 3$ below about $\eta \approx 7$ (assuming scaling values as above of $\dot{\epsilon}_g = 10^{-14}$ s^{-1} and $\eta_g = 10^{22}$ Pa s). At $\eta = 50$, the size of the pressure shadow that experiences pressures above 100 MPa is about $L/8$. The size of the pressure shadow within which 10 MPa is exceeded is larger. For $\eta = 50$ the distance, where pressure experiences 10 MPa is $\approx 1.7L$ at $n = 1$ and $1L$ for $n = 3$.

In order to compare the results of the *non-linear* rheologies with those of the linear case we compare them when the integrated shear stresses along the model boundaries ($\bar{\sigma}_{xy}$ at $y = 0.5$ and $y = -0.5$) are the same for both rheologies. As all numerical experiments were performed with the same velocity boundary conditions, this implies that the results were scaled by the factor:

$$F = \bar{\sigma}_{xy(n=1;y=0.5)} / \bar{\sigma}_{xy(n\neq 1;y=0.5)}.$$

For example, if in the linear case $\bar{\sigma}_{xy(n=1;y=0.5)} = 1$ on the shear zone boundary and $\bar{\sigma}_{xy(n=3;y=0.5)} = 1.3$ for $n = 3$, then all non-linear stresses for $n = 3$ were scaled by the factor 1/1.3 in the Figs. 3, 5 and 6, which may now be compared directly.

Fig. 5 shows that, for $n = 3$ and 5 (and assuming scaling values as above of $\dot{\epsilon}_g = 10^{-14}$ s^{-1} and $\eta_g = 10^{22}$ Pa s), $P_{\max}$ in the pressure shadow reaches 120 and 80 MPa, respectively. These pressures are 66 and 44% of those reached in linear viscous materials, respectively.

The distance where 10 or 100 MPa of pressure in the pressure shadow is exceeded (as shown in Fig. 6(b)) also decreases for increasing n. For the 10 MPa distance the shift between the three curves for $n = 1$, 3 and 5 is larger than for the 100 MPa distance for a given η.

4.1.1. Geological magnitude of η

The geological scaling discussed above depends on the strain rate and on the viscosity. The former is known to vary in the geologically relevant range of $\dot{\epsilon}_g = 10^{-12}$ s^{-1} to $\dot{\epsilon}_g = 10^{-15}$ s^{-1}. The latter is not very well known, but

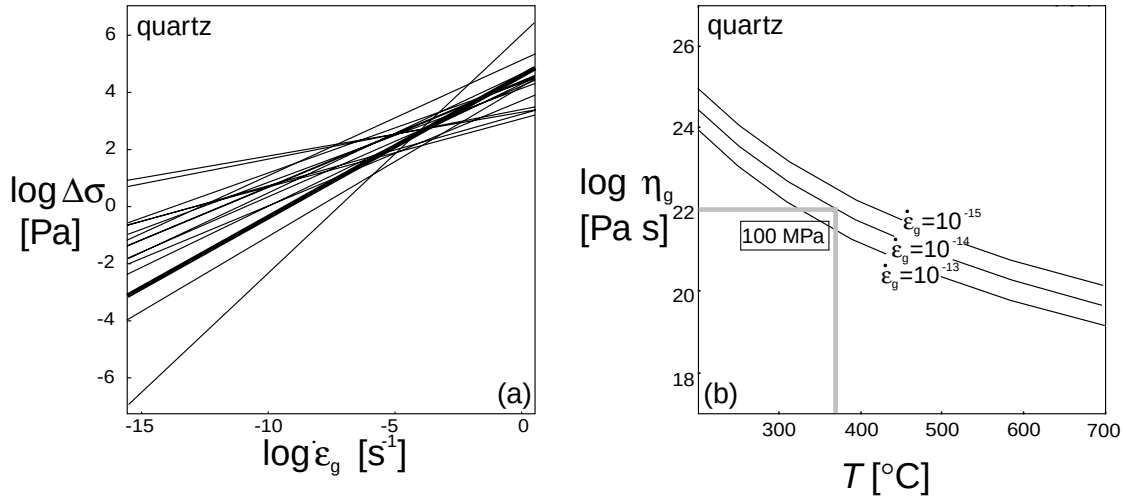

Fig. 7. (a) Comparison of different experimental data for quartz from the literature in a stress–strain rate diagram. In this diagram, the slope of the curves is n and the intercept is (ln}$(A) - Q/RT$) from (Eq. (6)) at 1000°C. Experimentally, A and Q are derived by carrying out experiments at different T. The examples are cited from Koch et al. (1989), Gleason and Tullis (1995), Carter and Tsenn (1986), Post et al. (1996) and Paterson and Luan (1990). (b) Effective viscosity of quartz as a function of temperature for three different strain rates. The following material constants (Shelton and Tullis, 1981) were used: $n = 2$, $A = 5 \times 10^{-5}$ MPa^{-n} s^{-1}, $Q = 134{,}000$ J mol^{-1}.

abundant studies have attempted to constrain rock viscosities using laboratory conditions that are then extrapolated to geologically reasonable temperatures and strain rates. Such laboratory experiments derive the material constants in terms of a power law of the general form:

$$\Delta\sigma = \left(\frac{\dot{\epsilon}_g}{A}\right)^{\frac{1}{n}} e^{\left(\frac{Q}{nRT}\right)} \quad (6)$$

where $\Delta\sigma = (\sigma_1 - \sigma_2)$, is the differential stress in Pa, $\dot{\epsilon}_g$ is strain rate in s^{-1}, A is a pre-exponent constant in Pa^{-n} s^{-1}, Q is the activation energy in J mol^{-1}, R is the gas constant, T is absolute temperature and n is the stress exponent. A series of experimental data for quartz and their relationship (Eq. (6)) are shown in Fig. 7(a). The thick line indicates the set of data (Shelton and Tullis, 1981), which was used to explore the magnitude of η in Fig. 7(b). According to England and McKenzie (1982) B in Eq. (2), is:

$$B = A^{-\frac{1}{n}} e^{\left(\frac{Q}{nRT}\right)} \text{ and } \eta_g = \frac{\Delta\sigma}{\dot{\epsilon}_g} = B\dot{\epsilon}_g^{\left(\frac{1}{n}-1\right)}. \quad (7)$$

In Fig. 7(b), the effective viscosity is shown for a range of temperatures and for three different strain rates. With increasing temperature, η_g decreases from about 10^{24} Pa s at 200°C to 10^{19} Pa s at 700°C for a given strain rate of $\dot{\epsilon}_g = 10^{-14}$ s^{-1}. For faster strain rates, η_g is smaller at the same temperature. For a temperature of ≈ 370°C (which is realistic for ductile deformation of quartz) and a strain rate of $\dot{\epsilon}_g = 10^{-14}$ s^{-1}, the effective viscosity η_g is 10^{22} Pa s and the pressure deviates by 100 MPa from lithostatic (shaded lines in Fig. 7(b)); however, the geological strain rates and viscosities can differ by 2 orders of magnitude. This also influences the geological pressures. For example, η_g for quartz is 10^{20} Pa s at 600°C for $\dot{\epsilon}_g = 10^{-14}$ s^{-1}. Therefore, pressure is only 10^6 Pa or 1 MPa different from lithostatic. In summary, for a geologically realistic range of strain rates and viscosities, the pressures in the pressure shadow can vary between 1 and 100 MPa pressure difference. For higher metamorphic conditions the local stress differences around rigid objects are likely to be smaller than for lower conditions.

4.2. The influence of object size

In our experiments we have followed Pennacchioni et al. (2000) and Masuda and Mizuno (1996) and have chosen an object size of $L = 0.2$ as a good approximation for the behaviour of the stress state of porphyroblasts in an infinitely wide shear zone. Strictly speaking, however, this is only true for $L \rightarrow 0$ where the distance of object to the shear zone boundaries, $D = (1 - L)/L$, goes towards infinity. Biermeier et al. (2000) showed that the rotation rate of cylindrical objects may be strongly dependent on D even for $L < 0.2$. Because of this problem, Masuda and Ando (1988) and Masuda and Mizuno (1996) forced a rotation rate of the cylindrical object, $\dot{\omega}$, to be $\dot{\omega} = \dot{\epsilon}_{xy}/2$ as part of their boundary conditions. This is the rotation rate of an object in an infinite matrix under simple shear (Ghosh, 1975; Jeffrey, 1922). Because of the discrepancies of the rotation rate *inforced* as a boundary condition by Masuda and Ando (1988) and the rotation rate *obtained* as a result by Biermeier et al. (2000) for the same L, it is necessary to re-investigate the robustness of the magnitude of pressure shadows as a function of L. We explored this function using P_{max} as an illustrative parameter, for a variety of boundary conditions.

Fig. 8 shows the influence of object size on P_{max} for linear rheologies. For the boundary conditions used above (continuous lines in Fig. 8) it may be seen that boundary

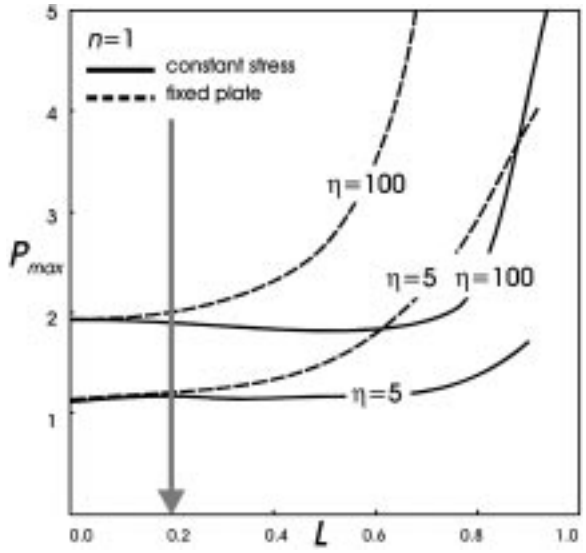

Fig. 8. The influence of the object size L on P_{max}, at $n = 1$. This relationship is shown for two different viscosity contrasts η and two different sets of boundary conditions approximating simple shear in the far field. The continuous lines are for the boundary conditions used in this paper, the dashed lines for 'fixed plate' boundary conditions. The shaded arrow marks the object size used in this paper.

effects become only significant for $L > 0.7$. This result is not very dependent of the viscosity contrast. Thus, the assumption of $L = 0.2$ is a safe approximation for $D \rightarrow \infty$. We also explored this influence for different non-linearities (not shown in Fig. 8) with the same result. Interestingly, the magnitude of pressure is much more robust to object size than the rotation rate (Biermeier et al., 2000).

We also investigated the magnitude of P_{max} for boundary conditions that approximate ideal simple shear better than those assumed in this paper. For this, we assumed 'fixed plate boundary conditions' (dashed lines in Fig. 8; see also, Bons et al., 1997). These differ from those used in this paper in that the y component of the boundary conditions at the top and bottom boundaries is defined by $u_y = 0$ (in contrast to the $\tau_{yy} = 0$ used for Figs. 3–6). These conditions approximate the conditions of shear box experiments or those of narrow shear zones of constant width. Fig. 8 shows that, for small L, P_{max} is the same for both sets of boundary conditions. This is because both the boundaries are effectively infinitely distant from the porphyroblast. For the 'fixed plate condition', however, the boundary conditions influence the pressure shadow for $L > 0.3$. The 'fixed plate' boundary conditions have a much stronger influence on the pressure shadow than the stress boundary conditions, because the limited space between fixed shear zone boundaries and cylindrical object strongly changes the stress pattern. For $L = 0.2$ (assumed in this paper) the difference in P_{max} for different boundary conditions is less than 5%. Thus, it is justified to interpret the results for $L = 0.2$ to be representative of the behaviour of pressure shadows around porphyroblasts in a matrix of infinite extent. We emphasise, however, that the magnitude of pressure shadows given in Figs. 3–6 is a minimum. If porphyroblasts in rocks are closer than $D = 4$ from the shear zone boundaries, the magnitude of pressure in the pressure shadows may increase dramatically.

4.3. Geological relevance

Three observation-related questions on pressure shadows around porpyroblasts in polyphase metamorphic rocks may be discussed in terms of the results presented in the last sections. (1) What is the significance of the size and geometry of pressure shadows in real rocks in terms of the results of Fig. 3? (2) What is the significance of the fact that pressure *shadows* are commonly observed, while pressure *highs* ('strain caps') in the opposite quadrants are much smaller in spatial extent? (3) What is the significance of the fact that the minerals that grow in pressure shadows around porphyroblasts are often products of metamorphic decompression reactions? This question arises as Figs. 4–6 suggest that *local*, rather than *lithostatic* decompression may be responsible for such reactions. In the following we discuss these questions individually.

4.3.1. Geological interpretation of the geometry

Figs. 3–6 suggest that it should be possible—in principle—to infer n and η from the geometry and size of pressure shadows in real rocks. These figures also suggest that pressure shadows in rocks should be 'bone-shaped'. In most natural rocks, however, 'pressure shadows' are triangular in shape and generally smaller than the porphyroblast near which they occur (Fig. 1a–c). Pressure fringes like that shown in Fig. 1(d) *are* 'bone-shaped', but do not form as a function of processes discussed here (for discussion of their formation see Köhn et al., 2000). We suggest that this is because what is loosely referred to as 'pressure shadows' is a feature that does *not* correspond to pressure. Rather, it is a zone of high or low strain, which is oriented obliquely to the pressure maxima and parallel to the shear zone boundaries (compare Fig. 3). In order to test the influence of finite deformation on the geometry and position of the incremental pressure shadow, we have performed a finite deformation experiment for which we assumed that a rheologically more viscous phase has grown in the incremental pressure shadow at the onset of deformation (Fig. 9(a)). The result is shown in Fig. 9(b).

During finite strain, the material of the matrix and the pressure shadow is coupled with the object and therefore rotated counterclockwise to form a weak δ-shape. This is shown in Fig. 9(b) around the left-hand porphyroblast, where the deformed shape of the phase assumed to have grown in the incremental pressure shadow of (a) is shaded. It may be seen that the two branches of the pressure shadow on the top right of the porphyroblast behave differently with increasing strain. While the upper branch is elongated during ductile flow, the lower branch is much less influenced by finite deformation. This is because, in the

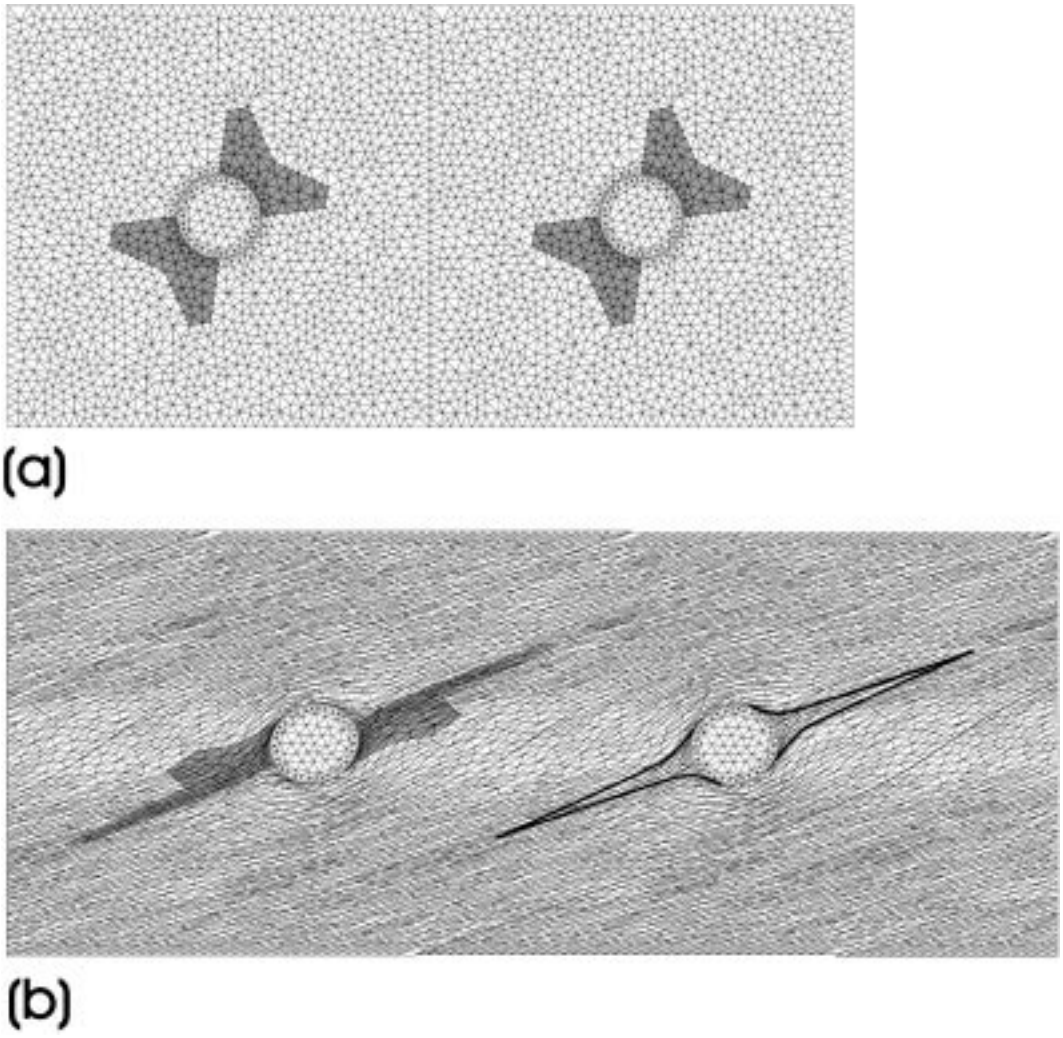

Fig. 9. Illustration of finite deformation of an incremental pressure shadow, which was instantaneously filled by a third phase at the incremental time step (grey-shaded region) ($n = 5$). (a) Initial situation (compare Fig. 3(c) for the shape of the pressure shadow). The two porphyroblasts have a viscosity contrast to the matrix of $\eta = 100$, while the phase grown in the pressure shadow is characterised by $\eta = 2$. (b) represents (a) after finite simple shear strain of 3. For illustration, the deformed shape of the phase grown in the incremental pressure shadow of (a) is shown for the left porphyroblast and the region of maximum strain accumulation is outlined (thick line) around the right hand porphyroblast.

horizontal direction on both sides of the porphyroblast, there is a zone of low strain rate. We define this zone as *strain rate shadow*, where the principle strain rate reaches a minimum. This zone is indicated by the horizontal band of coarse triangulation in Fig. 9(b). With increasing strain, the two branches may coalesce, parallel to the finite flow direction—this may correspond to the triangular shape which can be observed in natural rocks. It is important to realise that both areas outlined in Fig. 9(b) (the deformed incremental pressure shadow on the left and the high strain zone on the right) are *not* the pressure shadow at the shown time step of finite deformation. This has a complicated shape because of the additional rheology contrast imposed by the phase grown in the incremental pressure shadow. We have also calculated an example of a rheologically weaker phase grown in the pressure shadow. Under these conditions the results show even better the effect of finite deformation on the distribution of material that has grown in the pressure shadows.

The equivalents to the pressure shadows in the opposite quadrants are the strain caps. The strain caps are equal in geometry and size but the magnitude is opposite in sign. Strain caps can firstly be the result of solution processes caused by local stress differences and therefore contain only the residual minerals that are not soluble. They can often be observed in low-grade rocks. For the correct interpretation of this kind of strain caps, it would be necessary to apply a flow law describing pressure-solution-precipitation-creep. Secondly, minerals are newly grown in the compressive quadrant around the porphyroblast (as shown in Fig. 1(a)). For these, the assumption of power law flow as the dominating deformation mechanism may be sufficient. The reason why strain caps occur smaller in thin sections may also be explained in terms of finite strain. Minerals that are

growing in the strain cap are continuously transported away by the flowing matrix, whereas the part of the pressure shadow that is located in the strain rate shadow also survives high strains, so the strain caps are often completely destroyed by high strain.

4.3.2. Geological evidence for local decompression

In Fig. 1(b), biotite is located preferentially in the pressure shadows behind garnet. In rocks with the peak paragenesis, garnet–muscovite–quartz is biotite a typical retrograde reaction product during decompression of the rocks from the metamorphic peak. Traditionally, this decompression reaction has been interpreted as a result of the decrease of the lithostatic stress during exhumation of rocks. However, in Fig. 1(b), biotite grows in the pressure shadows around garnet at the expense of muscovite, while muscovite in the matrix is often unaffected by this reaction. Thus, it is possible that the growth of biotite is related to a local decompression around the rigid garnet and not to a decrease in lithostatic stress. For the bulk composition of the rock in Fig. 1(b) it has been shown that for every 100 MPa of decompression the volumetric proportions of biotite increases by about 5 vol% on the expense of about 2 vol% muscovite and 1 vol% garnet (Stüwe and Powell, 1995; Tenczer and Stüwe, 1999). This will be within the pressure differences of Fig. 7 and therefore indicates that finite strain does not influence the magnitude of the pressure in the pressure shadow as much as it influences the geometry. Stüwe and Sandiford (1994) have also shown that the crust can support deviatoric stresses of up to about 100 MPa and that localised decompression can result in 'clockwise' P–T paths while other regions show 'anti-clockwise' P–T evolution. Therefore, P–T paths that are based on a few points in P–T space without the contribution of the textural relationship may not represent the real history of the rock during metamorphism. The question that arises now is how to translate the pressure gradients that do exist around circular rigid objects into reaction gradients, which has not been performed until now. Based on this finite element simulation done with BASIL, the program package ELLE (www.earth.monash.edu.au/Research/Elle) will have the ability to contribute to the application of pressure gradients onto reaction gradients to solve questions of respective field examples and contribute to answering the question of the role of differential stress during the history of tectono-metamorphic events.

5. Conclusions

1. The geometry of the pressure shadows around circular porphyroblasts is a function of the stress exponent n but independent of the rheology contrast between object and matrix. It is roughly circular in shape for $n = 1$, but disintegrates into two branches for $n > 1$ so that it becomes 'bone-shaped' at geologically relevant $n = 3$ or 5.
2. The magnitude of the pressure in the pressure shadow is a function of both the viscosity contrast and n, even at large viscosity contrasts. Thus, it is conceivable that different pressures may be measured in pressure shadows behind different porphyroblasts, if these have a different rheology. This effect is true up to high rheology contrasts and becomes even stronger at high n.
3. Scaling of pressures with experimentally-derived material constants leads to a large spread of pressure over several orders of magnitude, for geologically reasonable strain rates and temperatures. Pressure deviations from the far field up to about 200 MPa, however, are easily possible at geologically relevant strain rates and viscosities. Therefore, care should be taken when interpreting barometric results in the vicinity of texturally-observed 'pressure shadows'.

Acknowledgements

G. Houseman developed the FEM package used in this study. His continued interest and support is gratefully acknowledged. This study would also have been impossible without the continuous help of L. Evans who did not get tired of implementing new tools into the FEM package BASIL for us to use. We also would like to thank D. Köhn for providing Fig. 1(d) as well as C. Biermeier and H. Fritz for their continued interest. The reviewers G. Dresen and S. Ji contributed with helpful comments. G. Humphreys derived the analytical solution presented in Appendix A and provided a great contribution in the final stage of this paper. This study was supported by FWF project P12846-GEO of the Austrian Science Foundation.

Appendix A

The numerical results presented in this paper may be compared with an analytical solution describing the pressure field around a circular rigid inclusion ($\eta \to \infty$) immersed in a Newtonian matrix. If we only consider the pressure as a function of distance from the inclusion along the r-axis (as we did in Figs. 4–6), the Navier Stokes equation (in polar coordinates) may be written as:

$$\frac{\delta P}{\delta r} = \eta\left(\frac{1}{r^2}\frac{\delta}{\delta r}\left(r^2\frac{\delta u_r}{\delta r}\right) - \frac{2u_r}{r^2}\right) \tag{8}$$

where the radial velocity is $u_r = \sqrt{u_x^2 + u_y^2}$ (from Turcotte and Schubert, 1982, Eq. 6-195). The radial flow along the r-axis for pure shear deformation is:

$$u_r = \frac{1}{2}\dot{\epsilon}_{xy}\frac{\left(r^2 - 1\right)^2}{r^3} \tag{9}$$

(from Cox et al., 1968, Eq. 12). Substituting Eq. (9) into Eq.

(8) leads to:

$$\frac{\delta P}{\delta r} = \frac{\dot{\epsilon}_{xy}\eta}{2}\left(\frac{4}{r^3} + \frac{4}{r^5}\right). \quad (10)$$

This gives the pressure gradient $\delta P/\delta r = 4\dot{\epsilon}_{xy}\eta$ at $r = 1$, which is the contact of the inclusion. Integrating Eq. (10) gives P as a function of r:

$$P = \frac{\dot{\epsilon}_{xy}\eta}{2}\left(\frac{2}{r^2} + \frac{1}{r^4}\right) \quad (11)$$

which satisfies $P \rightarrow 0$ on $r \rightarrow \infty$. From Eq. (11), the maximum pressure at the contact of the inclusion (at $r = 1$) is given by:

$$P_{\max} = \tfrac{3}{2}\dot{\epsilon}_{xy}\eta. \quad (12)$$

The simple solution presented above does *not* consider rotation of the inclusion, nor does it consider simple shear deformation. Both, however, may be neglected because—in Newtonian rheologies—solutions for rotational and distortional components of deformation may be superimposed and the rotational component is not associated with a pressure field.

References

Barr, T.D., Houseman, G.A., 1996. Deformation fields around a fault embedded in a non-linear ductile medium. Geophysical Journal International 125, 473–490.

Biermeier, C., Stüwe, K., Barr, T.D., 2001. The rotation rate of cylindrical objects during simple shear. Journal of Structural Geology 23, 765–776.

Bons, P.D., Barr, T.D., ten Brink, C.E., 1997. The development of (-clasts in non-linear viscous materials: a numerical approach. Tectonophysics 270, 29–41.

Carter, N.L., Tsenn, M.C., 1987. Flow properties of continental lithosphere. Tectonophysics 136, 27–63.

Cox, R.G., Zia, I.Y.Z., Mason, S.G., 1968. Particle motions in sheared suspensions. Journal of Colloid and Interface Science 27, 7–18.

Edward, G.H., Etheridge, M.A., Hobbs, B.E., 1982. On the stress dependence of subgrain size. Textures and Microstructures 5, 127–152.

England, P., McKenzie, D., 1982. A thin viscous sheet model for continental deformation. Geophysical Journal of the Royal Astronomical Society 70, 295–321.

Ernst, W.G., 1971. Do mineral parageneses reflect unusually high pressure conditions of Franciscan metamorphism?. American Journal of Science 270, 81–108.

Frost, H.J., Ashby, M.F., 1982. Deformation Mechanism Maps. Pergamon Press, Oxford 167pp.

Ghosh, S.K., 1975. Distortion of planar structures around rigid spherical bodies. Tectonophysics 18, 185–208.

Gleason, G.C., Tullis, J., 1995. A flow law for dislocation creep of quartz aggregates determined with the molten salt cell. Tectonophysics 247, 1–23.

Jeffrey, G.B., 1922. The motion of ellipsoidal particles immersed in a viscous fluid. Proceedings of the Royal Society London 102, 161–179.

Ji, S., Martignole, J., 1994. Ductility of garnet as an indicator of extremely high temperature deformation. Journal of Structural Geology 16, 985–996.

Kenkmann, T., 2000. Processes controlling the shrinkage of porphyroclasts in gabbroic shear zones. Journal of Structural Geology 22, 471–478.

Kenkmann, T., Dresen, G., 1998. Stress gradients around porphyroclasts: palaeopiezometric estimates and numerical modelling. Journal of Structural Geology 20, 163–173.

Koch, P.S., 1983. Rheology and microstructures of experimentally deformed quartz aggregates. Ph.D. Dissertation, University of California, Los Angeles, 464pp.

Koch, P.S., Christie, J.M., Ord, A., George, R.P., 1989. Effect of water on the rheology of experimentally deformed quartzite. Journal of Geophysical Research 94, 13975–13996.

Köhn, D., Hilgers, C., Bons, P.D., Passchier, C.W., 2000. Numerical simulation of fibre growth in antitaxial strain fringes. Journal of Structural Geology 22, 1311–1324.

Mancktelow, N.S., 1993. Tectonic overpressure in competent mafic layers and the development of isolated eclogites. Journal of Metamorphic Geology 11, 801–812.

Masuda, T., Ando, S., 1988. Viscous flow around a rigid spherical body: a hydrodynamical approach. Tectonophysics 148, 337–346.

Masuda, T., Mizuno, N., 1996. Deflection of non-Newtonian simple shear flow around a rigid cylindrical body by the finite element method. Journal of Structural Geology 18, 1089–1100.

Masuda, T., Mizuno, N., Kobayashi, M., Ngoc Nam, T., Otoh, S., 1995. Stress and strain estimates for Newtonian and non-Newtonian materials in a rotational shear zone. Journal of Structural Geology 17, 451–454.

McKenzie, D., Holness, M., 2000. Local deformation in compacting flows: development of pressure shadows. Earth and Planetary Science Letters 180, 169–184.

Passchier, C.W., Trouw, R.A.J, 1996. Microtectonics. Springer-Verlag, Berlin-Heidelberg.

Paterson, M.S., Luan, F.C., 1990. Quartzite rheology under geological conditions. In: Knipe, R.J., Rutter, E.H. (Eds.). Deformation Mechanisms, Rheology and Tectonics. , pp. 299–307 Geological Society Special Publication 54.

Pennacchioni, G., Fasolo, L., Cecchi, M.M., Salasnich, L., 2000. Finite-element modelling of simple shear flow in Newtonian and non-Newtonian fluids around a circular rigid particle. Journal of Structural Geology 22, 683–692.

Petrini, K., Podladchikov, Y., 2000. Lithospheric pressure–depth relationship in compressive regions of thickened crust. Journal of Metamorphic Geology 18, 67–78.

Post, A.D., Tullis, J., Yund, R.A., 1996. Effects of chemical environment on dislocation creep of quartzite. Journal of Geophysical Research 101, 22143–22155.

Rutland, R.W.R., 1965. Tectonic overpressures. In: Pitcher, W.S., Flynn, G.W. (Eds.). Controls of Metamorphism. Verl. Oliver and Boyd, Edinburgh, pp. 119–139.

Selkman, S.O., 1983. Stress and displacement distribution around pyrite grains. Journal of Structural Geology 5, 47–52.

Selkman, S.O., 1978. Stress and displacement analyses of boudinages by the finite-element method. Tectonophysics 44, 115–139.

Shelton, G.L., Tullis, J., 1981. : Experimental flow laws for crustal rocks. EOS, Transactions of the American Geophysical Union 62, 396.

Shimamoto, T., 1975. The finite element analysis of the deformation of a viscous spherical body embedded in a viscous medium. Journal of the Geological Society of Japan 81, 255–267.

Strömgård, K.E., 1973. Stress distribution during formation of boudinage and pressure shadows. Tectonophysics 16, 215–248.

Strömgård, K.E., 1974. Stress-induced diffusion during folding. Tectonophysics 22, 233–251.

Stüwe, K., Powell, R., 1995. PT paths from modal proportions. Applications to the Koralm Complex, Eastern Alps. Contributions to Mineralogy and Petrology 119, 83–93.

Stüwe, K., Sandiford, M., 1994. Contribution of deviatoric stresses to metamorphic P–T paths: an example appropriate to low-P, high-T metamorphism. Journal of Metamorphic Geology 12, 445–454.

Tenczer, V., Stüwe, K., 1999. Some constraints on strength and rheology of the Plattengneiss shear zone (Koralm–Austroalpine). Mitteilungen des Naturwissenschaftlichen Vereins für Steiermark 129, 43–53.

Turcotte, D.L., Schubert, G., 1982. Geodynamics. Applications of Continuum Physics to Geological Problems. John Wiley and Sons, New York, p. 264.